

UC Berkeley

UC Berkeley Previously Published Works

Title

Unexpected Diffusion Anisotropy of Carbon Dioxide in the Metal–Organic Framework Zn<sub>2</sub>(dobpdc)

Permalink

<https://escholarship.org/uc/item/3xd3z5rz>

Journal

Journal of the American Chemical Society, 140(5)

ISSN

0002-7863

Authors

Forse, Alexander C  
Gonzalez, Miguel I  
Siegelman, Rebecca L  
et al.

Publication Date

2018-02-07

DOI

10.1021/jacs.7b09453

Peer reviewed

# Unexpected Diffusion Anisotropy of Carbon Dioxide in the Metal–Organic Framework $Zn_2(\text{dobpdc})$

Alexander C. Forse,<sup>†,‡,§,Ⓢ</sup> Miguel I. Gonzalez,<sup>†</sup> Rebecca L. Siegelman,<sup>†</sup> Velencia J. Witherspoon,<sup>‡,Ⓢ</sup> Sudi Jawahery,<sup>‡,Ⓢ</sup> Rocio Mercado,<sup>‡</sup> Phillip J. Milner,<sup>†</sup> Jeffrey D. Martell,<sup>†</sup> Berend Smit,<sup>†,‡,Ⓢ,||</sup> Bernhard Blümich,<sup>⊥</sup> Jeffrey R. Long,<sup>\*,†,‡,‡,Ⓢ,Ⓢ</sup> and Jeffrey A. Reimer<sup>\*,†,‡,‡,Ⓢ</sup>

<sup>†</sup>Department of Chemistry, <sup>‡</sup>Department of Chemical and Biomolecular Engineering, and <sup>§</sup>Berkeley Energy and Climate Institute, University of California, Berkeley, California 94720, United States

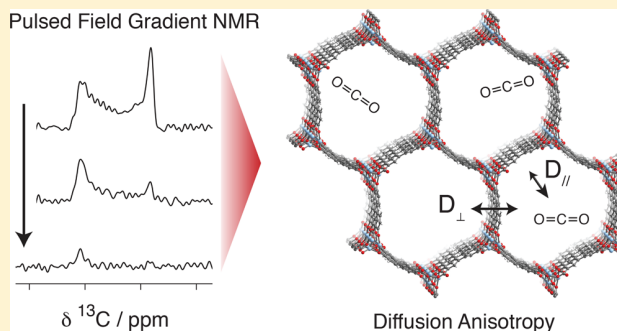
<sup>||</sup>Institut des Sciences et Ingenierie Chimiques, Valais, École Polytechnique Fédérale de Lausanne (EPFL), Rue de l'Industrie 17, CH-1951 Sion, Switzerland

<sup>⊥</sup>Institut für Technische und Makromolekulare Chemie (ITMC), RWTH Aachen University, 52062 Aachen, Germany

<sup>#</sup>Materials Sciences Division, Lawrence Berkeley National Laboratory, Berkeley, California 94720, United States

## Supporting Information

**ABSTRACT:** Metal–organic frameworks are promising materials for energy-efficient gas separations, but little is known about the diffusion of adsorbates in materials featuring one-dimensional porosity at the nanoscale. An understanding of the interplay between framework structure and gas diffusion is crucial for the practical application of these materials as adsorbents or in mixed-matrix membranes, since the rate of gas diffusion within the adsorbent pores impacts the required size (and therefore cost) of the adsorbent column or membrane. Here, we investigate the diffusion of  $\text{CO}_2$  within the pores of  $Zn_2(\text{dobpdc})$  ( $\text{dobpdc}^{4-} = 4,4'$ -dioxidobiphenyl-3,3'-dicarboxylate) using pulsed field gradient (PFG) nuclear magnetic resonance (NMR) spectroscopy and molecular dynamics (MD) simulations. The residual chemical shift anisotropy for pore-confined  $\text{CO}_2$  allows PFG NMR measurements of self-diffusion in different crystallographic directions, and our analysis of the entire NMR line shape as a function of the applied field gradient provides a precise determination of the self-diffusion coefficients. In addition to observing  $\text{CO}_2$  diffusion through the channels parallel to the crystallographic  $c$  axis (self-diffusion coefficient  $D_{\parallel} = (5.8 \pm 0.1) \times 10^{-9} \text{ m}^2 \text{ s}^{-1}$  at a pressure of 625 mbar  $\text{CO}_2$ ), we unexpectedly find that  $\text{CO}_2$  is also able to diffuse between the hexagonal channels in the crystallographic  $ab$  plane ( $D_{\perp} = (1.9 \pm 0.2) \times 10^{-10} \text{ m}^2 \text{ s}^{-1}$ ), despite the walls of these channels appearing impermeable by single-crystal X-ray crystallography and flexible lattice MD simulations. Observation of such unexpected diffusion in the  $ab$  plane suggests the presence of defects that enable effective multidimensional  $\text{CO}_2$  transport in a metal–organic framework with nominally one-dimensional porosity.



## INTRODUCTION

Synthetic porous materials such as metal–organic frameworks (MOFs) show great potential for energy-efficient gas separations. A key advantage of MOFs compared to traditional porous materials, such as carbons and zeolites, is their highly tunable chemistry, porosity, and topology, which allow the targeted design of materials for particular separations. Frameworks in the MOF-74 family,<sup>1</sup> such as  $M_2(\text{dobdc})$  ( $\text{dobdc}^{4-} = 2,5$ -dioxido-1,4-benzenedicarboxylate;  $M = \text{Mg, Mn, Fe, Co, Ni, Cu, Zn, Cd}$ )<sup>1–8</sup> and the expanded variants  $M_2(\text{dobpdc})$  ( $\text{dobpdc}^{4-} = 4,4'$ -dioxidobiphenyl-3,3'-dicarboxylate;  $M = \text{Mg, Mn, Fe, Co, Ni, Zn}$ )<sup>9–11</sup> in particular demonstrate promise for the separation of  $\text{CO}_2$  from simulated fossil fuel flue gas mixtures<sup>12–14</sup> as well as for  $\text{CO}_2/\text{CH}_4$  separations.<sup>15</sup> These frameworks feature one-dimensional hexagonal channels lined with a high density of coordinatively unsaturated metal

centers (see Figure 1), and their  $\text{CO}_2$  capture performance has been found to improve dramatically upon appending diamines to the metal sites. The diamine-appended frameworks cooperatively adsorb  $\text{CO}_2$  via the formation of ammonium carbamate chains, resulting in a dramatically improved performance in the presence of water as well as low regeneration energies.<sup>9,10,16–20</sup>

Despite the promise of MOF-74 materials for a variety of gas separations, an understanding of gas diffusion in this class of materials is lacking. The importance of strong  $\text{CO}_2$ –metal interactions in dictating local energy barriers for diffusive motion between different binding sites in  $Mg_2(\text{dobdc})$  has previously been highlighted.<sup>21</sup> Nuclear magnetic resonance

Received: September 4, 2017

Published: January 4, 2018

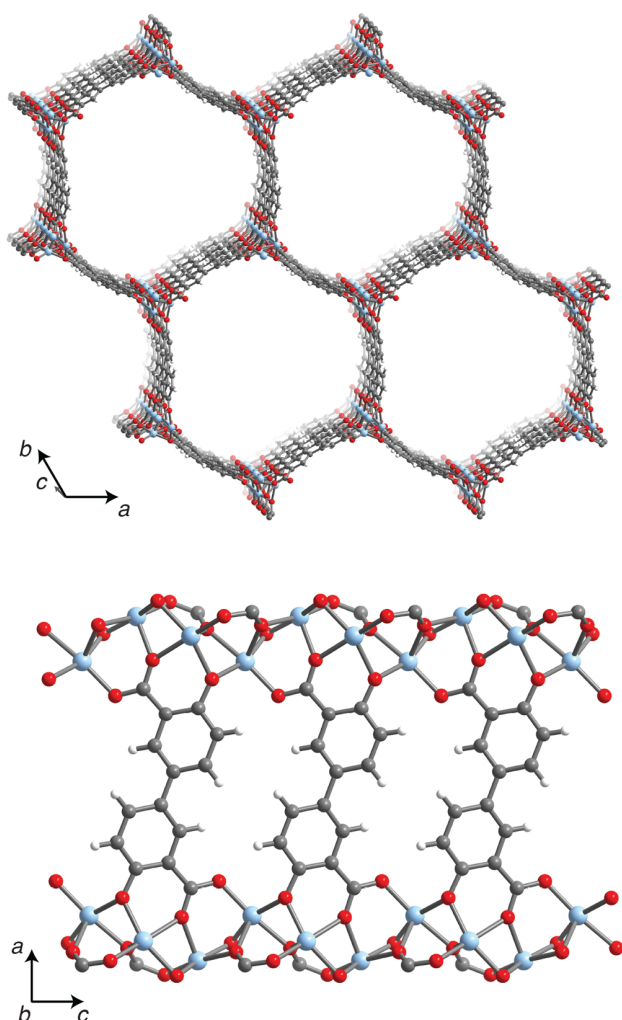


**Figure 1.** A portion of the crystal structure of  $\text{Zn}_2(\text{dobpdc})$  at 298 K shown from two different perspectives, as determined by single-crystal X-ray diffraction. Light blue, red, gray, and white spheres represent Zn, O, C, and H atoms, respectively.

(NMR) spectroscopy has also been used to probe the hopping dynamics and resulting average orientations of  $\text{CO}_2$  molecules in the pores of  $\text{Mg}_2(\text{dobdc})$  via the measurement of residual chemical shift anisotropies.<sup>22,23</sup> Despite this progress, little is known about the long-range diffusive motion of molecules within materials of this type. In particular, the magnitude and directionality of gas diffusion within the one-dimensional nanosized pores of these adsorbents are poorly understood, even though such parameters have a substantial impact on their practical utility. By understanding gas diffusion in this class of MOFs, we hope to guide the design of new materials with improved gas transport properties.

Pulsed-field gradient (PFG) NMR spectroscopy allows the measurement of self-diffusion coefficients of pore-confined molecules<sup>24–30</sup> and uses pulses of magnetic field gradients to encode and decode the positions of the molecules. In this technique, a series of NMR experiments are first carried out with magnetic field gradient pulses of increasing strength, and self-diffusion coefficients are subsequently obtained by fitting the decay of the NMR signal intensity as a function of the field gradient.<sup>31</sup> PFG NMR spectroscopy is an attractive means of characterization, as it can also be used to measure diffusion

anisotropy.<sup>31–34</sup> For example, aligning single crystals of a material at different orientations relative to the magnetic field gradient direction (the direction in which diffusion is measured) allows one to probe the diffusion of adsorbed molecules in different crystallographic directions.<sup>35–37</sup> An alternative approach that does not require oriented single crystals is to make use of residual anisotropic NMR interactions in static polycrystalline samples, wherein the resonance frequency is dependent on the crystallite orientation. Using the latter approach, residual quadrupole interactions ( $^2\text{H}$  NMR) combined with PFG experiments have been used to measure the diffusion anisotropy of  $^2\text{H}_2\text{O}$  in a polycrystalline liquid crystal sample.<sup>36</sup> Later studies employed similar approaches based on residual chemical shift anisotropies.<sup>37–39</sup> In particular, the qualitative analysis of powder line shapes for  $\text{CO}_2$  adsorbed in a metal–organic framework can be used to determine the preferred crystallographic direction for self-diffusion.<sup>39,40</sup>

Here, we utilize the residual chemical shift anisotropy of  $\text{CO}_2$  confined in the nanopores of  $\text{Zn}_2(\text{dobpdc})$  to extract the diffusion anisotropy as a function of gas pressure. The large single crystals of this material (up to  $\sim 750 \mu\text{m}$  in length) facilitate the measurement of diffusion of the pore-confined gas molecules, because exchange with the gas outside of the pores is negligible under the experimental conditions. Our quantitative analysis of the evolution of the entire spectral line shape with increasing pulsed field gradient strength offers precise determination of self-diffusion coefficients parallel and perpendicular to the hexagonal channels. Molecular dynamics (MD) simulations and *in situ* single-crystal X-ray diffraction measurements are employed as aides in trying to understand the results.

## RESULTS AND DISCUSSION

**NMR Spectra of  $^{13}\text{CO}_2$ -Dosed  $\text{Zn}_2(\text{dobpdc})$ .** The reaction of  $\text{Zn}(\text{NO}_3)_2 \cdot 6\text{H}_2\text{O}$  and  $\text{H}_4\text{dobpdc}$  at  $100^\circ\text{C}$  for 2 days<sup>17</sup> yielded needle-like crystals of  $\text{Zn}_2(\text{dobpdc})$  (Figure 2, see also Figure 1). Successively washing the crystals with *N,N*-dimethylacetamide, methanol, and toluene, followed by activation for 12 h at  $250^\circ\text{C}$  under flowing Ar, yielded crystals with lengths of up to  $750 \mu\text{m}$  and widths of up to  $120 \mu\text{m}$  (Figure 2b, Figure S1), which were then used to prepare NMR samples.

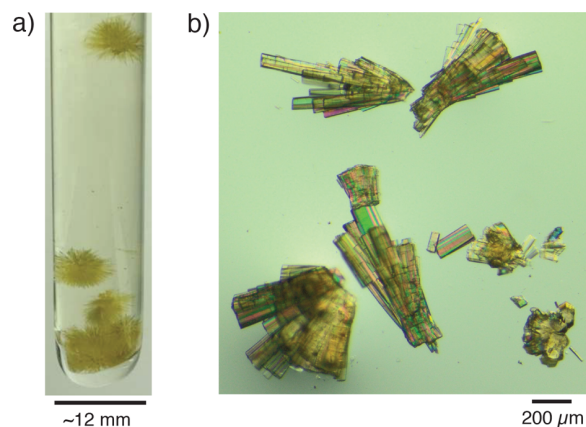


**Figure 2.** (a) Photograph of as-synthesized crystals of  $\text{Zn}_2(\text{dobpdc})$  inside a sealed tube. (b) Microscope image of crystals in air following washing and activation.

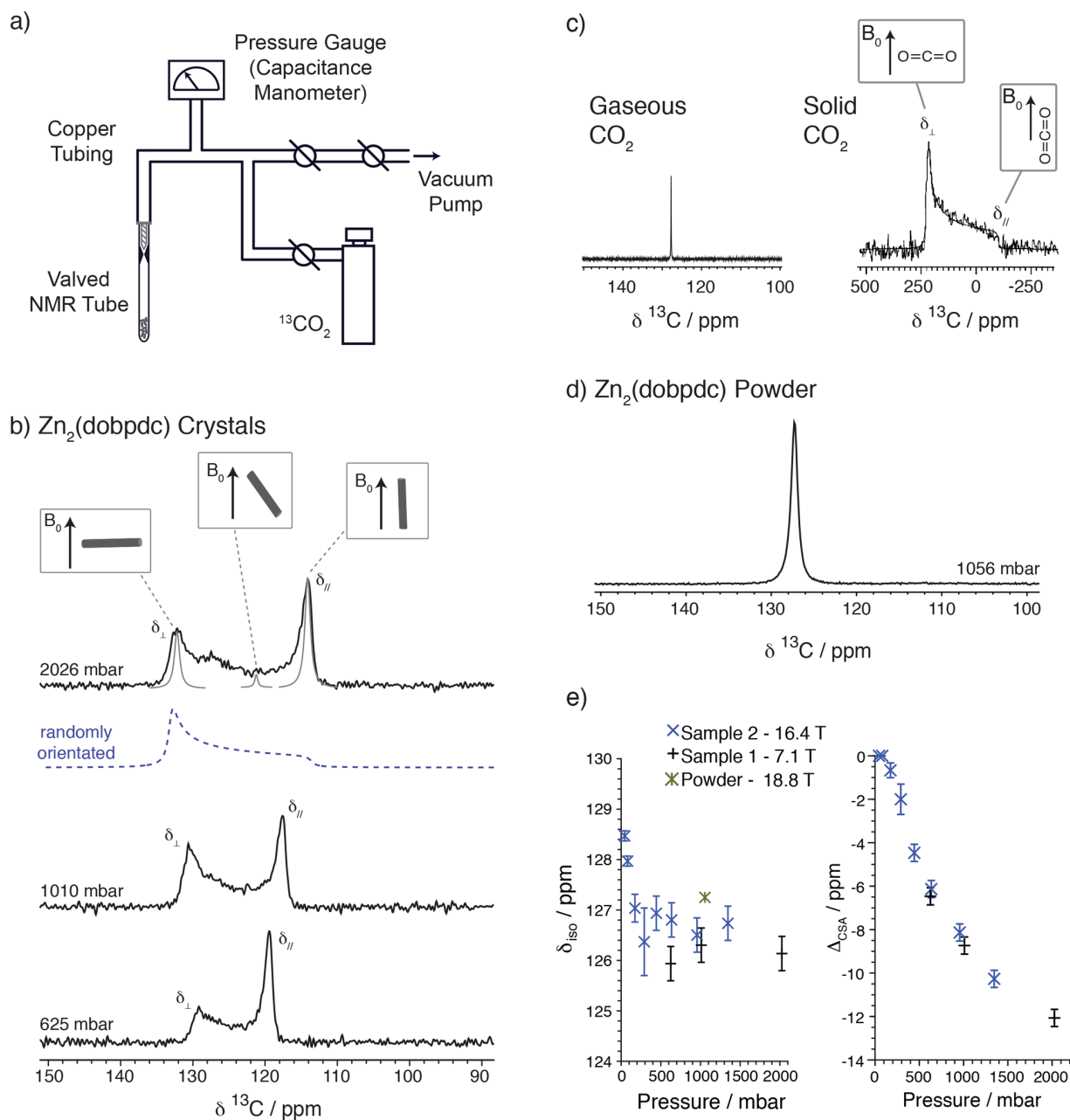


**Figure 3.** (a) Custom-built gas dosing apparatus for preparing  $^{13}\text{CO}_2$ -dosed NMR samples. (b) Static  $^{13}\text{C}$  NMR (7.1 T) spectra of  $\text{Zn}_2(\text{dobpdc})$  crystals (sample 1) dosed with  $^{13}\text{CO}_2$  at different pressures ( $T = 25^\circ\text{C}$ ). Dashed blue line shows the predicted line shape at 2026 mbar for randomly orientated crystals. Gray peaks indicate schematically the spectral contributions from crystals with different orientations. (c) Static  $^{13}\text{C}$  NMR spectra of gaseous (1 bar) and solid  $\text{CO}_2$  (no adsorbent present), the latter is adapted from ref 41 with permission of Elsevier. (d)  $^{13}\text{C}$  NMR (18.8 T) spectrum of  $\text{Zn}_2(\text{dobpdc})$  powder dosed with 1056 mbar  $^{13}\text{CO}_2$  ( $T = 22^\circ\text{C}$ ). (e) Pressure dependence of NMR parameters extracted from spectra on two independent samples, sample 1 and sample 2 (which were studied at different magnetic field strengths) and a powder sample,  $\delta_{\text{iso}} = (2\delta_{\perp} + \delta_{\parallel})/3$  and  $\Delta_{\text{CSA}} = \delta_{\parallel} - \delta_{\text{iso}}$ .

The  $\text{Zn}_2(\text{dobpdc})$  crystals were dosed *ex situ* with  $^{13}\text{CO}_2$  using a custom-built gas dosing manifold (Figure 3a). Static  $^{13}\text{C}$  NMR spectra of these crystals exhibit a feature that can be assigned to  $\text{CO}_2$  confined within the pores of the framework (Figure 3b). Measurements of the  $\text{CO}_2$  adsorption isotherm and integrated NMR signal intensities from 0 to 2026 mbar of  $\text{CO}_2$  (Figure S2) indicate occupancies of up to 0.9  $\text{CO}_2$  molecules per metal site at the highest studied pressure. An unusual powder pattern line shape is apparent in the NMR spectra, with the overall width depending on the gas pressure.

Previously reported  $^{13}\text{C}$  NMR spectra for solid  $\text{CO}_2$  and our measured spectrum for gaseous  $\text{CO}_2$  (Figure 3c) provide a useful reference here.<sup>41</sup> In the gas phase, isotropic molecular rotation yields a narrow resonance at the isotropic chemical shift,  $\delta_{\text{iso}} = 127.7$  ppm. In the solid state,  $\text{CO}_2$  exhibits a significant chemical shift anisotropy ( $\Delta_{\text{CSA}}$ ), arising from the highly anisotropic shape of the molecule. For solid  $\text{CO}_2$ ,  $\Delta_{\text{CSA}} = \delta_{\parallel} - \delta_{\text{iso}}$  is approximately  $-210$  ppm, where  $\delta_{\text{iso}} = (2\delta_{\perp} + \delta_{\parallel})/3$ , and intensity at  $\delta_{\perp}$  arises from  $\text{CO}_2$  molecules that are oriented perpendicular to the applied magnetic field ( $B_0$ ), while intensity

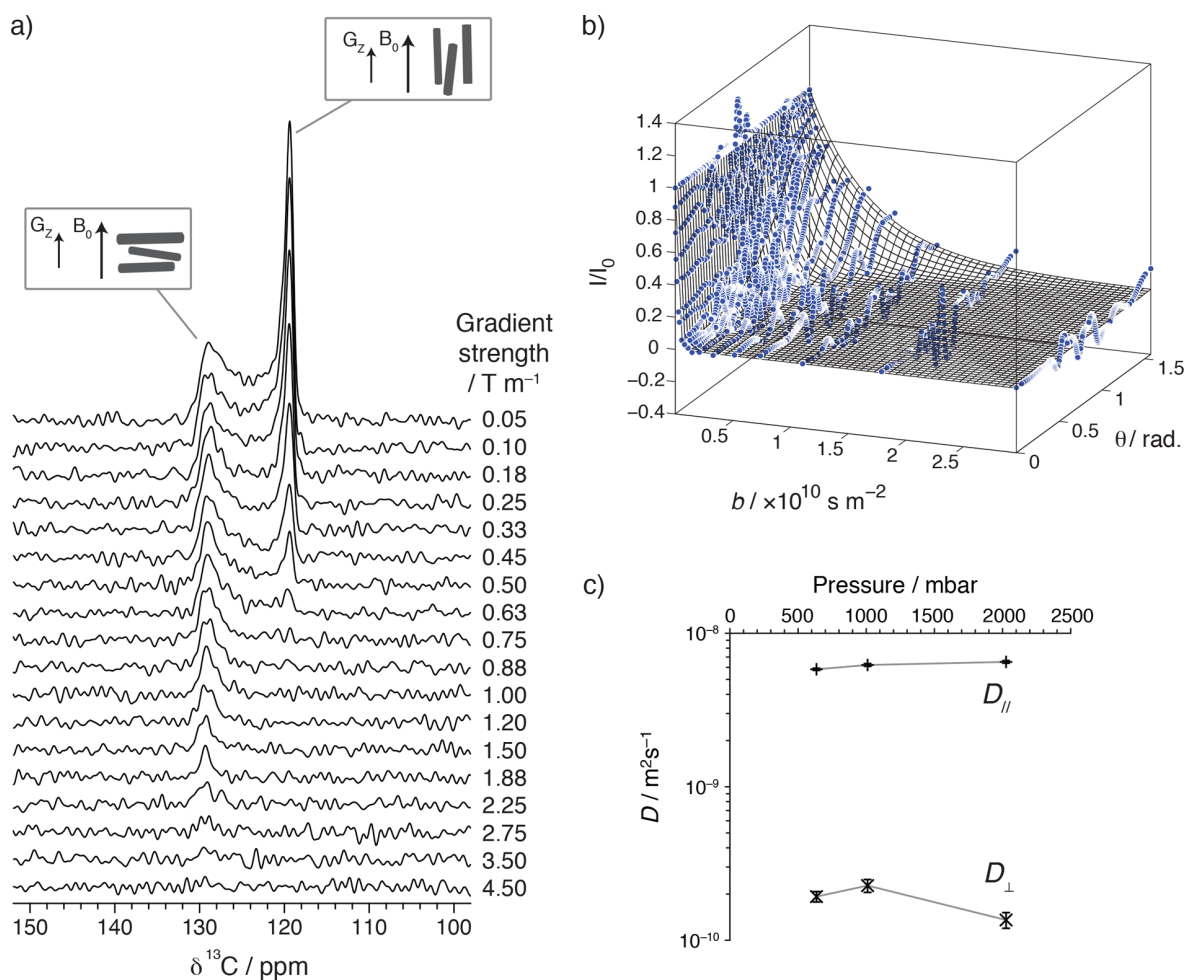


**Figure 4.** (a) PFG NMR (7.1 T) spectra for  $\text{Zn}_2(\text{dobpdc})$  crystals (sample 1) at a pressure of 625 mbar  $^{13}\text{CO}_2$  with different applied gradient strengths ( $T = 25$  °C). (b) Data and fit for results shown in panel a with PFG NMR signal decays shown as a function of crystal orientation,  $\theta$ . The fit is represented as a meshed surface. Data points are shown as blue circles and are normalized to 1 for  $g = 0.05 \text{ T m}^{-1}$  for all crystal orientations (note that this normalization results in more noisy data at intermediate  $\theta$  values where absolute signal intensities are weaker, due to the small number of crystals at these orientations). (c) Self-diffusion coefficients obtained at 25 °C for  $\text{Zn}_2(\text{dobpdc})$  crystals (sample 1) dosed with different pressures of  $^{13}\text{CO}_2$ . The errors in these values arise from uncertainty in the fitting procedure and represent 95% confidence limits.

at  $\delta_{\parallel}$  arises from  $\text{CO}_2$  molecules oriented parallel to the applied field.

Pore-confined  $\text{CO}_2$  in  $\text{Zn}_2(\text{dobpdc})$  crystals exhibits a residual chemical shift anisotropy. In this regime, crystals with different orientations relative to  $B_0$  exhibit different chemical shifts for confined  $\text{CO}_2$  molecules. This effect arises because the molecular reorientation inside the pores is *not* isotropic, and  $\text{CO}_2$  has preferred *average* orientations relative to the crystal frame (Figure 3b). We stress that it is the different orientations of the *crystals* relative to  $B_0$  that give rise to the observed spread of chemical shifts in Figure 3b. While the metal is the primary binding site for  $\text{CO}_2$  in these materials,<sup>14</sup>  $\text{CO}_2$  undergoes translations between different metal sites on the NMR time scale, and a symmetric narrow line is thus expected for a single crystal (reflecting the average environment of pore-confined  $\text{CO}_2$  on a millisecond time scale; see below for more details).<sup>22,42</sup> We note that similar line shapes for confined  $\text{CO}_2$  have previously been observed in other (noncubic) MOFs,<sup>39,40,43–47</sup> including the isorecticular framework  $\text{Mg}_2(\text{dobdc})$ .<sup>22,42</sup>

We hypothesize that intensity at the left-hand edge of the spectrum arises from  $\text{CO}_2$  inside the pores of crystals that are oriented perpendicular to the magnetic field ( $B_0$ ) direction and intensity at the right-hand edge arises from  $\text{CO}_2$  in the pores of crystals that are oriented parallel to the field direction (Figure 3b). With this assumption, the calculated  $\Delta_{\text{CSA}}$  ( $= \delta_{\parallel} - \delta_{\text{iso}}$ ) values are negative. The observed line shapes deviate significantly from that expected for a randomly oriented polycrystalline powder sample (shown as a dashed blue line in Figure 3b). This deviation arises because the large crystal sizes result in a partial macroscopic alignment of their long axis with the long axis of the NMR tube, leading to additional intensity at  $\delta_{\parallel}$ . Consistent with this observation, we find that physical shaking of the crystal samples results in marked changes of intensity in different regions of the spectra (Figure S3).

Our assignments of  $\delta_{\perp}$  and  $\delta_{\parallel}$  are supported by four pieces of evidence. First, magic angle spinning (MAS) spectra collected for gas-dosed single crystals (Figure S4) yield a negative chemical shift anisotropy, as well as an isotropic chemical shift consistent with our assignments. Second, measurements of

Zn<sub>2</sub>(dobpdc) powder dosed with <sup>13</sup>CO<sub>2</sub> (Figure 3d, see Experimental Section for powder synthesis) yield a narrow resonance with an isotropic chemical shift consistent with our assignments (see Figure 3e). Interestingly, a residual chemical shift anisotropy is not visible in this spectrum, suggestive either of fast chemical exchange between different crystallites (typical crystallite lengths are <15 μm, and widths are <2 μm; see Figure S5) or that the preferred orientation of CO<sub>2</sub> relative to the crystal frame is slightly different in the powder and the crystal samples, which were synthesized via different routes. Third, the sign of the assigned Δ<sub>CSA</sub> agrees with that calculated by MD simulations (see below). Finally, the diffusion behavior observed below is consistent with our assignments, with D<sub>||</sub> ≫ D<sub>⊥</sub> as anticipated. An alternative assignment of the spectra in Figure 3b would be that intensity at the left-hand edge arises from crystals that are parallel to B<sub>0</sub> and that intensity at the right-hand edge arises from crystals that are perpendicular to B<sub>0</sub> (i.e., positive Δ<sub>CSA</sub>). However, we reject this alternative assignment, as it is inconsistent with the four observations above.

The graphs in Figure 3e show the variations of Δ<sub>CSA</sub> and δ<sub>iso</sub> with <sup>13</sup>CO<sub>2</sub> pressure. These data are in agreement within error for two independent samples measured at different field strengths, which we call “sample 1” and “sample 2” (see Figure S6 for spectra of sample 2, collected with *in situ* dosing). Notably, δ<sub>iso</sub> shows small variations at lower pressures and then appears to plateau at higher pressures, while the magnitude of Δ<sub>CSA</sub> increases continuously with pressure (see below for discussion of this).

**Anisotropic Diffusion of CO<sub>2</sub>.** PFG NMR measurements of sample 1 dosed *ex situ* with 625 mbar of <sup>13</sup>CO<sub>2</sub> are shown in Figure 4a. In these measurements, magnetic field gradient pulses were applied along the laboratory z-direction (i.e., parallel to B<sub>0</sub>; see Figure S7). Upon application of pulsed magnetic field gradients of increasing magnitude, the right-hand edge of the spectrum decays more rapidly than the left-hand edge. Face-indexing of a single crystal confirmed that the c-axis (and therefore the one-dimensional pores) runs along the long axis of the needle-like Zn<sub>2</sub>(dobpdc) crystals. Using this observation and our prior assignments of the spectra (Figure 3b), we can obtain CO<sub>2</sub> self-diffusion coefficients both parallel (D<sub>||</sub>) and perpendicular (D<sub>⊥</sub>) to the hexagonal channels of Zn<sub>2</sub>(dobpdc).

The observed chemical shift, δ, for pore-confined CO<sub>2</sub> in a crystal oriented at an angle (θ) relative to B<sub>0</sub> is given by

$$\begin{aligned}\delta(\theta) &= \delta_{\text{iso}} + \frac{\Delta_{\text{CSA}}}{2}(3 \cos^2 \theta - 1) \\ &= \delta_{\parallel} \cos^2(\theta) + \delta_{\perp} \sin^2(\theta)\end{aligned}\quad (1)$$

The effective self-diffusion coefficient (D) measured using magnetic field gradients in the z-direction depends on θ in a similar way and is given by<sup>32</sup>

$$D(\theta) = D_{\parallel} \cos^2(\theta) + D_{\perp} \sin^2(\theta)\quad (2)$$

Finally, the decay of signal intensity (I), normalized by the intensity for zero gradient (I<sub>0</sub>), is given by

$$\frac{I}{I_0} = \exp[-bD(\theta)]\quad (3)$$

The constant b is proportional to the square of the gradient strength (g) and also depends on the gyromagnetic ratio (γ) of

the studied nucleus and a number of experimental parameters (see Figure S8 for definitions of Δ, δ', τ) and is given by

$$b = g^2(2\delta'\gamma)^2\left(\Delta - \frac{\delta'}{6} - \frac{\tau}{2}\right)\quad (4)$$

The self-diffusion coefficients D<sub>||</sub> and D<sub>⊥</sub> are therefore the only free parameters in the fit to the data in Figure 4b using eq 3. Here, we fit against all of the data (i.e., I/I<sub>0</sub> vs b across all crystal orientations, θ) simultaneously to obtain diffusion coefficients with relatively small uncertainties. This analysis method is preferred to individual fits of integrated signal intensities across a small range of chemical shifts, which revealed similar results but with errors at least three times larger due to uncertainty in the fits. The dominant source of error in our analysis is most likely systematic error arising from the finite peak line widths that arise from homogeneous broadening, such that for a given δ, crystals at a range of θ values contribute to the signal.<sup>33,37</sup> Indeed, this is evidenced by an apparent narrowing of the signal at δ<sub>⊥</sub> at the largest applied gradient strengths (Figure 4a). This arises from the signal decay for CO<sub>2</sub> in crystals with orientations, θ, close to but unequal to 90°. We note that it would be interesting to carry out PFG NMR with different gradient orientations.<sup>39</sup> Under such conditions the form of the PFG NMR decays would differ and could further improve the accuracy of our diffusion measurements.

A global fit to eq 3 (Figure 4b) affords D<sub>||</sub> = (5.8 ± 0.1) × 10<sup>-9</sup> m<sup>2</sup> s<sup>-1</sup> and D<sub>⊥</sub> = (1.9 ± 0.2) × 10<sup>-10</sup> m<sup>2</sup> s<sup>-1</sup>. These values suggest that the self-diffusion of CO<sub>2</sub> is ~30 times faster along the hexagonal channels compared to diffusion between the channels at this pressure. It is surprising that gas diffusion perpendicular to the channels is possible at all, given the apparent lack of pore windows between neighboring channels in the ab plane, as judged from the crystal structure (see below). We note that the measured values are of similar order to self-diffusion values of bulk liquids, though they are more than 3 orders of magnitude smaller than the self-diffusion coefficient of gaseous CO<sub>2</sub> (1.1 × 10<sup>-5</sup> m<sup>2</sup> s<sup>-1</sup> at 25 °C, 1 bar).<sup>48</sup> Our measured values are of similar order to the diffusion of CO<sub>2</sub> in other large-pore MOFs, such as HKUST-1 (D = 1.7 × 10<sup>-9</sup> m<sup>2</sup> s<sup>-1</sup>),<sup>49</sup> Zn<sub>2</sub>(bdc)<sub>2</sub>(dabco) (D<sub>||</sub> = 1.1 × 10<sup>-8</sup> m<sup>2</sup> s<sup>-1</sup> and D<sub>⊥</sub> = 3.7 × 10<sup>-9</sup> m<sup>2</sup> s<sup>-1</sup>),<sup>39</sup> and MIL-47(V) (D = 10<sup>-8</sup>–10<sup>-9</sup> m<sup>2</sup> s<sup>-1</sup>, depending on loading level).<sup>50</sup>

Because these PFG NMR experiments probe diffusion on length scales on the order of tens of micrometers, D<sub>⊥</sub> is the effective self-diffusion coefficient as CO<sub>2</sub> moves between thousands of pores, rather than within a single pore (a length scale that is inaccessible by this technique). Furthermore, for the observation times (Δ) studied here, the experiments probe diffusion in the pore-confined phase. Indeed, the root-mean-square displacements (RMSDs) of confined CO<sub>2</sub> in our experiments are smaller than the typical crystal dimensions (Figure 2b, Figure S1). The RMSD is calculated using the expression (nDΔ)<sup>0.5</sup> (n = 2 for diffusion in the c-direction and n = 4 for diffusion in the ab plane). For example, given Δ = 80 ms, the RMSDs are 30 μm along the c axis, and 8 μm in the ab plane, values that are smaller than the typical crystal lengths (hundreds of micrometers) and widths (tens of micrometers), respectively (Figure S1). Furthermore, diffusion coefficients measured for different Δ in the range of 20–160 ms show minimal variation, indicating that exchange of pore-confined CO<sub>2</sub> with CO<sub>2</sub> outside of the pores is not significant at these time scales (Figure S9). Exchange spectroscopy additionally

reveals that significant exchange of  $^{13}\text{CO}_2$  between crystals occurs on time scales of hundreds of milliseconds, much longer than the time scales employed here (Figure S10). In contrast, PFG NMR measurements on the powdered sample (typical crystallite lengths up to  $15\ \mu\text{m}$ , widths up to  $2\ \mu\text{m}$ ; Figure S5) yield much larger effective self-diffusion values, on the order of  $10^{-7}$ – $10^{-8}\ \text{m}^2\ \text{s}^{-1}$ , reflecting the more rapid exchange of  $\text{CO}_2$  between different crystallites as well as rapid diffusion in the intercrystallite space. Indeed, the probed RMSDs in this experiment are between  $\sim 100$ – $300\ \mu\text{m}$  for a relatively short observation time of 20 ms, highlighting the need for large crystals to reliably measure intracrystalline diffusion coefficients.

Further PFG NMR experiments on samples dosed at different  $^{13}\text{CO}_2$  gas pressures yielded similar results (see PFG NMR spectra and fits in Figures S11 and S12). The measured diffusion parameters at pressures of 635, 1010, and 2026 mbar are shown in Figure 4c and Table 1. The diffusion values appear

**Table 1. Self-Diffusion Coefficients of  $^{13}\text{CO}_2$  in  $\text{Zn}_2(\text{dobpdc})$  at 298 K**

pressure, mbar	$D_{\parallel}$ , $\text{m}^2\ \text{s}^{-1}$	$D_{\perp}$ , $\text{m}^2\ \text{s}^{-1}$	$D_{\parallel}/D_{\perp}$
635	$5.8(\pm 0.1) \times 10^{-9}$	$1.9(\pm 0.2) \times 10^{-10}$	$30 \pm 3$
1010	$6.2(\pm 0.2) \times 10^{-9}$	$2.3(\pm 0.3) \times 10^{-10}$	$27 \pm 4$
2026	$6.5(\pm 0.2) \times 10^{-9}$	$1.4(\pm 0.2) \times 10^{-10}$	$48 \pm 7$

relatively constant at these pressures, a result that is perhaps unsurprising given the relatively small variations in  $\text{CO}_2$  loading in the pressure range investigated (see  $\text{CO}_2$  adsorption isotherm in Figure S2a).

**Molecular Dynamics Simulations.** To further probe  $\text{CO}_2$  diffusion in  $\text{Zn}_2(\text{dobpdc})$ , we performed MD simulations using (i) a fully flexible MOF lattice model and (ii) a rigid MOF lattice. Figure 5a shows the time-evolution of the mean square displacement (MSD) of  $\text{CO}_2$  molecules in the different crystallographic directions for the flexible lattice model with a  $\text{CO}_2$  pressure of 1 bar. Since  $\log(\text{MSD})$  is given by  $\log(nD) + \log(t)$  in the diffusive regime, a slope of 1 and a  $y$ -intercept of  $\log(nD)$  are anticipated on a log–log plot, provided that sufficiently long times are probed to reach this regime. Inspection of the plot in Figure 5a thus informs an assessment of the diffusion behavior of  $\text{CO}_2$  in  $\text{Zn}_2(\text{dobpdc})$ .

Long-range self-diffusion of  $\text{CO}_2$  occurs along the  $c$  axis, as anticipated, with the diffusive regime (slope = 1) being reached at times longer than  $\sim 10$  ps (Figure 5a). In contrast, diffusion of  $\text{CO}_2$  in the  $ab$  plane is limited to displacements within a single pore, with no diffusive jumps occurring between different channels. This observation is reflected by the apparent plateauing of the MSD in the  $ab$  plane at long times, with the diffusive regime never being reached. At 298 K, the MSD climbs to  $\sim 160\ \text{\AA}^2$  at a time of 10 ns, corresponding to a RMSD of  $\sim 13\ \text{\AA}$ , which, as expected, is less than the pore diameter of  $\sim 22\ \text{\AA}$ .

Similar behavior is apparent at all three studied temperatures of 298, 400, and 500 K, as well as at a lower pressure of 0.01 bar (Figure S13a), indicating the absence of a thermally activated diffusion mechanism that could allow  $\text{CO}_2$  to move between pores. MD simulations with a rigid lattice also revealed the absence of long-range diffusion in the  $ab$  plane. This observation from MD simulations, which is based upon the assumption of perfect crystals, is in contrast to the results from PFG NMR experiments, where crystal defects may affect  $\text{CO}_2$  diffusion (see below).

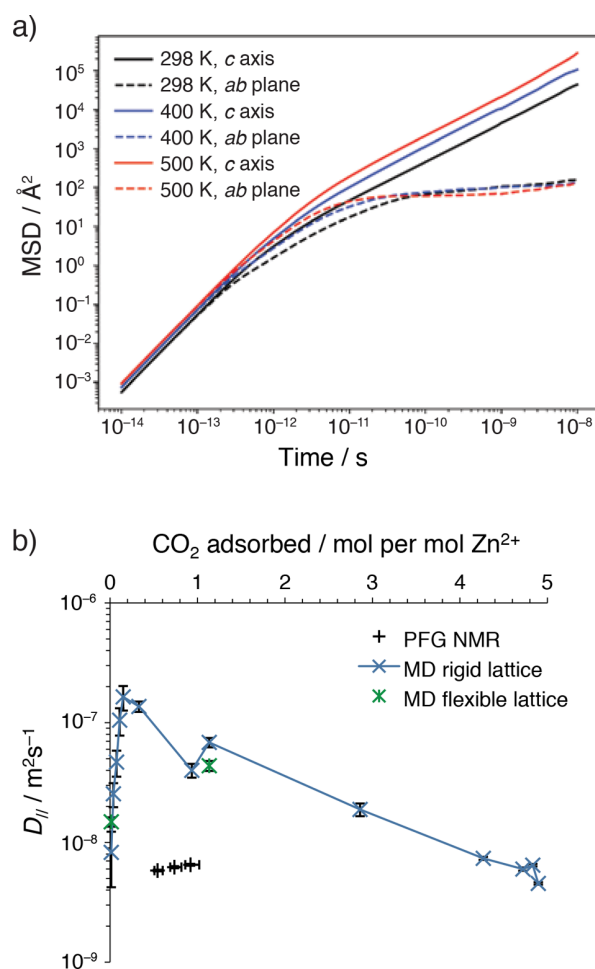


**Figure 5.** (a) MSDs in different crystallographic directions from flexible MOF MD simulations at 298, 400, and 500 K and a  $\text{CO}_2$  pressure of 1 bar. Individual one-dimensional MSDs were calculated for the  $a$  and  $b$  directions, and the average is shown in the plot. (b) Self-diffusion coefficients (298 K) along the  $c$  axis ( $D_{\parallel}$ ) at a range of pressures. Values are shown for rigid and flexible lattice MD simulations as well as those obtained using PFG NMR. The amount of  $\text{CO}_2$  adsorbed for the PFG NMR samples was estimated from Figure S2a. See Figure S13b for a plot of  $D_{\parallel}$  against  $\text{CO}_2$  pressure.

The self-diffusion coefficients along the  $c$  axis ( $D_{\parallel}$ ) determined from MD simulations are shown in Figure 5b and Figure S13b. These simulations allow access to pressures from 10 mbar to 100 bar (a much wider range of pressures, and therefore  $\text{CO}_2$  loadings, than is accessible with our current NMR apparatus) and reveal loading-dependent diffusion behavior. A clear increase in  $D_{\parallel}$  is observed at very low loadings, followed by decreases at higher loadings. We postulate that at the lowest loadings, the small  $D_{\parallel}$  values result from the high density of open metal sites. Indeed, DFT calculations of  $\text{CO}_2$  diffusion pathways in a similar MOF,  $\text{Mg}_2(\text{dobdc})$ , have shown that the energy barrier for  $\text{CO}_2$  to move from a metal site to a neighboring unoccupied metal site is  $\sim 300$  meV ( $\sim 30$  kJ mol $^{-1}$ ).<sup>21</sup> After some of the metal sites become occupied by  $\text{CO}_2$ , additional lower energy pathways may give rise to the observed increase in  $D_{\parallel}$ , particularly diffusive motion of  $\text{CO}_2$  through the pore center, which bypasses interaction with metal sites that are already occupied by other  $\text{CO}_2$  molecules (for  $\text{Mg}_2(\text{dobdc})$ , a barrier  $< 40$  meV or  $> 4$  kJ mol $^{-1}$ ).<sup>21</sup> The

availability of these additional pathways is exemplified by the upturn in  $D_{\parallel}$  between 750 and 1000 mbar, which also corresponds to the point at which a loading of 1 CO<sub>2</sub> per Zn<sup>2+</sup> site is surpassed in the simulations. At higher CO<sub>2</sub> loadings, the observed decreases in  $D_{\parallel}$  are due to CO<sub>2</sub>–CO<sub>2</sub> interactions. We note that PFG NMR gives smaller self-diffusion values than MD by a factor of  $\sim 10$ , with such discrepancies not uncommon in the literature.<sup>51,52</sup> In the present case, differences in the experimental and simulated values may arise from both the presence of crystal defects in the experiment and small errors in the parametrization of the force field used for simulations.

The MD simulations also allow a prediction of the chemical shift anisotropy parameter,  $\Delta_{\text{CSA}}$ . We assume that the observed chemical shift is dependent only on the molecular orientation of CO<sub>2</sub> relative to the applied magnetic field and that framework–CO<sub>2</sub> interactions do not significantly perturb the chemical shift. This is a reasonable assumption given that our experimentally observed isotropic chemical shifts do not deviate significantly from that observed for free CO<sub>2</sub> gas (Figure 3e). Furthermore, we assume that CO<sub>2</sub> molecules exchange rapidly between different adsorption sites within the pores, such as primary sites (metal-bound) and secondary sites (not directly metal-bound) on the NMR time scale. Following a previously published procedure,<sup>40,53</sup> we first obtain probability distributions for the molecular orientations of CO<sub>2</sub> molecules in the crystal frame from the MD trajectories. We then obtain motionally averaged chemical shift tensors by performing a weighted average using the orientation probability distributions (see Supporting Information for details). Predicted  $\Delta_{\text{CSA}}$  values are then obtained from these tensors and are compared to the reported values for solid CO<sub>2</sub>,<sup>41</sup>  $\Delta_{\text{CSA,solid}}$ , as the order parameter  $\Delta_{\text{CSA}}/\Delta_{\text{CSA,solid}}$  (Table 2).

**Table 2.**  $\Delta_{\text{CSA}}$  Values for <sup>13</sup>CO<sub>2</sub> in Zn<sub>2</sub>(dobpdc) at 298 K from MD Simulations and NMR Spectroscopy (Sample 1)

method	pressure, mbar	$\Delta_{\text{CSA}}$ , ppm	$\Delta_{\text{CSA}}/\Delta_{\text{CSA,solid}}$
MD	750	−51.4	0.24
	1000	−51.5	0.25
	7500	−54.9	0.26
NMR	625	−6.5	0.03
	1010	−8.7	0.04
	2026	−12.1	0.06

Consistent with the NMR experiments, negative  $\Delta_{\text{CSA}}$  values are obtained that increase in magnitude with pressure (Table 2). The values show reasonable agreement, with the discrepancies similar to those in a related study.<sup>40</sup> The values from MD are systematically larger in magnitude than the NMR values. This disagreement likely arises from the presence of crystal defects that will affect the orientations of the CO<sub>2</sub> molecules in the pores. Our observed increase of the magnitude of  $\Delta_{\text{CSA}}$  with pressure is consistent with recent NMR measurements on the related metal–organic framework Mg<sub>2</sub>(dobdc).<sup>23</sup> The observed increases in  $|\Delta_{\text{CSA}}|$  with pressure likely reflect a competition between two factors: (i) the preferred orientation of CO<sub>2</sub> strongly interacting with Zn<sup>2+</sup> in primary adsorption sites and (ii) the occupation of secondary binding sites with a range of different orientations. At low pressures, the majority of CO<sub>2</sub> is bound in primary binding sites (see X-ray measurements below) and factor i will tend to dominate. At higher CO<sub>2</sub> pressures, an increasingly large

population of CO<sub>2</sub> in secondary sites is present in the pores, and factor ii becomes increasingly important.

**X-ray Crystallography.** To further explore the observed CO<sub>2</sub> diffusion behavior and the nonzero value of  $D_{\perp}$  from PFG NMR, we used *in situ* single-crystal X-ray diffraction to investigate the structure of Zn<sub>2</sub>(dobpdc) before (Figures 1 and S14) and after (Figure 6) exposure to 1.01 bar CO<sub>2</sub> at 298 K. Activated Zn<sub>2</sub>(dobpdc) is isostructural with previously reported solvated structures (Figure 1),<sup>9,17</sup> and no clear distortions of the framework are evident following the adsorption of CO<sub>2</sub> (Figure 6).

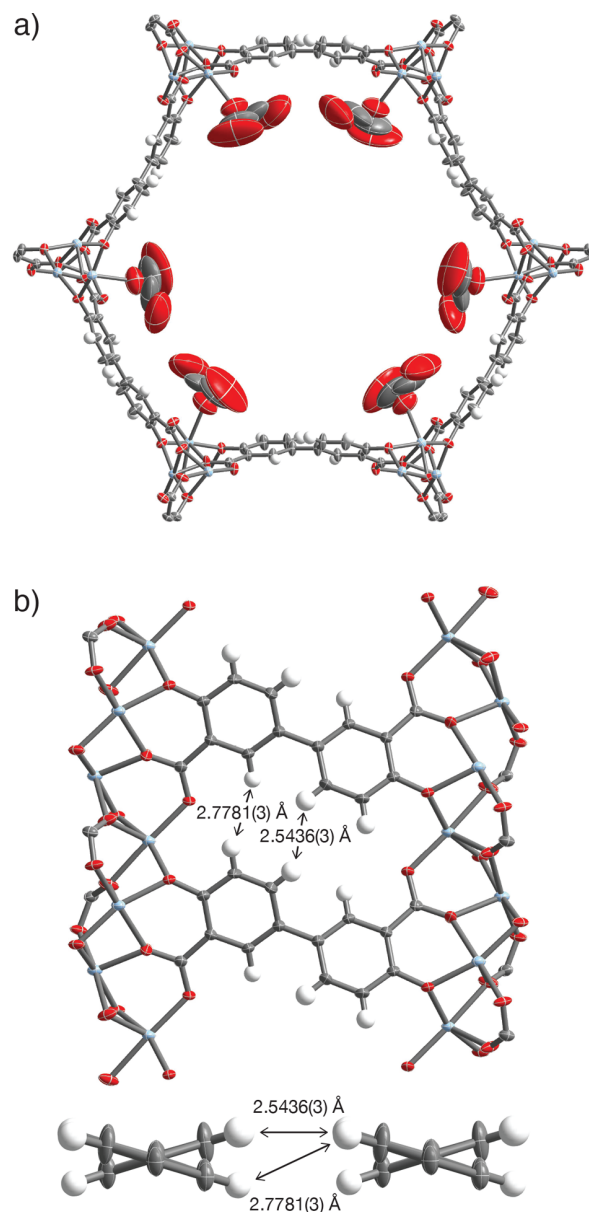


**Figure 6.** Views of the structure of Zn<sub>2</sub>(dobpdc) under 1.01 bar CO<sub>2</sub> obtained from single-crystal X-ray diffraction at 298 K. Light blue, red, gray, and white ellipsoids represent Zn, O, C, and H atoms, respectively. Note that CO<sub>2</sub> was found to be disordered over two orientations with occupancies of 34% and 30%. Thermal ellipsoids are drawn at a 50% probability level. In panel b, CO<sub>2</sub> atoms are omitted to enable a clear view of the pore walls.

We further examined the framework structure to determine if CO<sub>2</sub> can pass through the small space between dobpc<sup>4-</sup> linkers in the *ab* plane (Figure 6b). The H...H separations between adjacent linkers are 2.5436(3) Å (central H atoms) and 2.7781(3) Å (outer H atoms). Taking the H atom van der Waals radius to be 1.1 Å,<sup>54</sup> the maximum pore size of ~0.6 Å is much smaller than the diameter of a CO<sub>2</sub> molecule (estimated as 3.4 Å, twice the van der Waals radius of carbon<sup>55</sup>), such that diffusion of CO<sub>2</sub> in the *ab* plane is not expected. There are thus two most likely causes of the unexpected diffusion in the *ab* plane: (i) dynamics or (ii) defects.

Thermal ellipsoids drawn at a 50% probability level are shown in Figure 6 to aid the visualization of framework dynamics. The ellipsoids of the framework atoms are relatively small under the experimental conditions at 298 K, suggesting that there is little movement of the framework atoms over the average of all unit cells. We note that coordination of three oxygen donors at each end of the dobpc<sup>4-</sup> to the metal chains (one bridging and one nonbridging carboxylate oxygen and one bridging aryloxide oxygen) restrain the linker, limiting the motion of the phenyl rings. This contrasts to other common MOF linkers such as bpdc<sup>2-</sup> (bpdc<sup>2-</sup> = biphenyl-4,4'-dicarboxylate) that only bind through carboxylate groups. In these frameworks, the phenyl groups of the linker are often free to rotate about the phenyl-carboxylate C-C bond, which results in large thermal ellipsoids even at 100 K.<sup>56</sup> Note that our crystallographic data does not rule out an activated process in which the framework distorts to allow CO<sub>2</sub> to pass through a transient pore, which would not be discernible by crystallography. However, the flexible lattice MD simulations (Figure 5a) reveal no evidence for such an activated process, even at temperatures as high as 500 K. We therefore conclude that framework dynamics are unlikely to be responsible for the nonzero *D*<sub>⊥</sub> value observed by PFG NMR spectroscopy.

A second explanation for diffusion between channels in the *ab* plane is the presence of crystal defects. For example, missing linkers or missing Zn<sup>2+</sup> ions could result in porosity in the *ab* plane that would otherwise be absent. Refinement of the occupancy of the Zn<sup>2+</sup> site relative to a fixed occupancy of the dobpc<sup>4-</sup> linkers suggests a slight deficiency of zinc, with 94.8(4)% and 96.8(4)% of the anticipated electron density observed for activated and CO<sub>2</sub>-dosed (1.01 bar) Zn<sub>2</sub>(dobpc), respectively. Inductively coupled plasma optical emission spectrometry (ICP-OES) also indicated a slight deficiency of zinc compared to the expected molecular formula. Although elemental analysis gave H and C mass ratios that agree with the expected values for Zn<sub>2</sub>(dobpc) within error (Table S2), we note that some types of defects may not lead to significant changes in the material stoichiometry. The nature of the possible defects in this class of frameworks remains an active area of investigation.

Returning to the X-ray diffraction experiments, the CO<sub>2</sub>-loaded structure (Figure 6) allows two preferred binding sites for CO<sub>2</sub> to be resolved. The primary adsorption site lies at the open Zn<sup>2+</sup> coordination sites of the framework. We find that the Zn-O<sub>CO<sub>2</sub></sub> distance is 2.528(12) Å, which is slightly longer than the distance of 2.43(4) Å determined by powder neutron diffraction from an earlier study of CO<sub>2</sub>-dosed Zn<sub>2</sub>(dobdc) at 10 K.<sup>14</sup> This disparity in the distances may arise from the large difference in data collection temperature for the two structures. By comparison, the most common Zn-O<sub>CO<sub>2</sub></sub> distance from our MD simulations at similar conditions (1 bar CO<sub>2</sub>, 298 K) is

2.8–2.9 Å. This is in reasonable agreement with the DFT calculations to which the MD force field was parametrized, though slightly longer than that from X-ray diffraction. From previous DFT calculations using a dispersion-corrected functional,<sup>57,58</sup> it was observed that the preferred Zn-O<sub>CO<sub>2</sub></sub> distance in Zn<sub>2</sub>(dobdc) is 2.7 Å, which is approximately 0.2 Å longer than the other equilibrium M-O<sub>CO<sub>2</sub></sub> distances calculated (M = Mg, Co, Fe, and Ni) and also slightly longer than that observed experimentally by diffraction. A systematic overestimation of the M-O<sub>CO<sub>2</sub></sub> distances from DFT calculations has been observed previously with the same dispersion-corrected functional.<sup>14</sup> The longer distance obtained from MD may also be partly accounted for by the relatively large thermal ellipsoid of the metal-bound oxygen in the X-ray diffraction structure (Figure 6a), which will tend to lengthen the Zn-O<sub>CO<sub>2</sub></sub> distance. The bound CO<sub>2</sub> molecule in our X-ray structure exhibits disorder over two orientations with Zn-O-C angles of 152(3)° and 122(3)° and occupancies of 34% and 30%, respectively (Figure 6a). These occupancies correspond to a total of 0.64 CO<sub>2</sub> molecules per Zn, which is similar to the value of 0.72 expected from the gas sorption isotherm (Figure S2). The discrepancy between the two values likely arises due to the presence of some CO<sub>2</sub> at secondary binding sites, which are not resolvable in the diffraction experiments carried out here but can be seen in our MD simulations (Figure S15). In the future, variable-pressure crystallographic experiments may help us to further understand the nature of the different binding sites, as has been performed for the smaller pore M<sub>2</sub>(dobdc) materials.<sup>14,59–61</sup>

## CONCLUSIONS

The foregoing results demonstrate how the residual chemical shift anisotropy for CO<sub>2</sub> confined in the pores of the metal-organic framework Zn<sub>2</sub>(dobpc) allows measurement of the diffusion anisotropy using PFG NMR spectroscopy. Surprisingly, we find that the pore-confined gas is able to diffuse between adjacent framework channels in the *ab* plane, with self-diffusion coefficients of *D*<sub>∥</sub> = (5.8 ± 0.1) × 10<sup>-9</sup> m<sup>2</sup> s<sup>-1</sup> and *D*<sub>⊥</sub> = (1.9 ± 0.2) × 10<sup>-10</sup> m<sup>2</sup> s<sup>-1</sup> at 298 K and a pressure of 625 mbar of CO<sub>2</sub>. Measurements at gas pressures between 625 and 2026 mbar yielded very similar diffusion values, while MD simulations showed significant variations of self-diffusion at more extreme pressures. *In situ* single-crystal X-ray diffraction experiments revealed no obvious structural distortions upon the adsorption of CO<sub>2</sub>, while flexible lattice MD simulations revealed no diffusion between different channels in the *ab* plane. These findings indicate that defects in the framework structure are likely responsible for the observed nonzero diffusion in the *ab* plane. The marked diffusion anisotropy opens considerable opportunities for crystal engineering for CO<sub>2</sub> capture as well as other gas storage and separation applications, both for adsorbents and mixed-matrix membranes. For example, one could tune the crystal shapes and sizes to optimize fast adsorption and desorption, while the possibility of orienting MOF crystals with anisotropic diffusion properties in membranes should also be explored. The approaches described herein should be readily applicable to other porous materials exhibiting anisotropic pore structures.

## EXPERIMENTAL SECTION

**Materials and Methods.** All manipulations were performed under an N<sub>2</sub> atmosphere in a VAC atmospheres glovebox or using standard

Schlenk techniques. The ligand  $H_4dobpdc$  was purchased from Hangzhou Trylead Chemical Technology Co.  $N,N$ -Dimethylacetamide (DMA) and methanol were dried over 3 Å molecular sieves and then degassed via three successive freeze–pump–thaw cycles. Toluene and  $N,N$ -dimethylformamide (DMF) were deoxygenated by purging with Ar for 1 h and dried using a commercial solvent purification system designed by JC Meyer Solvent Systems. All other reagents were purchased from commercial sources and used without further purification. Adsorption isotherms for  $CO_2$  and  $N_2$  were obtained by volumetric methods using a Micromeritics ASAP 2020 gas adsorption analyzer. All gases were 99.998% purity or higher. The  $CO_2$  isotherm recorded at 25 °C was measured using a circulating water bath. The  $N_2$  isotherm at 77 K was measured using a liquid nitrogen bath. Laboratory powder X-ray diffraction patterns were collected using a Bruker AXS D8 Advance diffractometer using  $Cu K\alpha$  radiation ( $\lambda = 1.5418 \text{ \AA}$ ). Elemental analysis (H, C, and N) was conducted using a PerkinElmer 2400 Series II combustion analyzer. Inductively Coupled Plasma Optical Emission Spectrometry (ICP-OES) was conducted using an ICP Optima 7000 DV instrument.

**Preparation of  $Zn_2(dobpdc)$  Single Crystals.** A previously reported method was used to produce  $Zn_2(dobpdc)$  crystals.<sup>17</sup> Briefly,  $H_4dobpdc$  (164.6 mg, 600.0  $\mu\text{mol}$ ) was dissolved in 20 mL of DMA, while  $Zn(NO_3)_2 \cdot 6H_2O$  (446.2 mg, 1500  $\mu\text{mol}$ ) was dissolved in 40 mL of a 1:1 (v/v) mixture of distilled water and ethanol. The two solutions were combined, and  $\sim 10$  mL aliquots were dispensed into 0.5 in. outer diameter borosilicate tubes. Each tube was subjected to three freeze–pump–thaw cycles and then flame-sealed. The sealed tubes were placed in an oven preheated to 100 °C and kept at that temperature for 2 days. The resulting pale yellow, needle-shaped crystals were collected and washed by soaking in excess dry DMA, dry methanol, and dry toluene (3 washes for each solvent, each wash for at least 2 h at room temperature) under an Ar atmosphere. The crystals for sample 1 were activated at 250 °C under flowing Ar for 12 h. For sample 2, a second 24 h activation period (at 250 °C under high vacuum) was carried out.

**Synthesis of  $Zn_2(dobpdc)$  Powder.** A 1 L three-neck round-bottom flask was charged with  $H_4dobpdc$  (2.74 g, 10.0 mmol),  $ZnBr_2 \cdot 2H_2O$  (8.35 g, 32.0 mmol), ethanol (250 mL), and DMF (250 mL). The mixture was deoxygenated by purging with dry Ar for 1 h. The resulting solution was heated with magnetic stirring for 12 h at 120 °C under an Ar atmosphere. After the reaction mixture was allowed to cool to room temperature, the solvent was decanted, and the resulting off-white microcrystalline powder was washed by soaking three times in 500 mL of dry DMF at 120 °C for 24 h, then soaking three times in 500 mL of dry methanol at 120 °C for 24 h. The methanol-solvated powder was then filtered under Ar via cannula and desolvated by heating under dynamic vacuum at 180 °C for 24 h to give fully desolvated  $Zn_2(dobpdc)$ . Yield: 1.94 g (48.4%). Langmuir surface area ( $N_2$ , 77 K): 3110  $\text{m}^2/\text{g}$ . The powder X-ray diffraction pattern of the material was found to match the pattern simulated from the single-crystal structure (see Figure S16).

**Single-Crystal X-ray Diffraction Experiments.** Activation and gas dosing of single crystals were performed using a custom-designed environmental gas cell modified from a previous system.<sup>61</sup> A single crystal was first mounted on a MiTeGen loop using a minimal amount of epoxy, taking care to avoid the ends of the rod-shaped crystals. The sample was then transferred to the environmental cell, which consists of a borosilicate capillary with a vacuum-tight O-ring seal and a Beswick ball valve for dosing. Within the cell, the crystal was desolvated for 1 h at an external temperature of 200 °C using an Oxford Cryosystems cryostream and a turbomolecular pump. After solving the structure to confirm the absence of residual solvent in the pores, the crystal was cooled to 298 K, and the activated structure was collected. The crystal was then dosed with 1.01 bar of  $CO_2$  to obtain the structure of  $Zn_2(dobpdc) \cdot 1.26CO_2$ .

Single-crystal X-ray diffraction data were collected at Beamline 11.3.1 at the Advanced Light Source, Lawrence Berkeley National Laboratory, using synchrotron radiation ( $\lambda = 0.7749 \text{ \AA}$ ) and a Bruker AXS D8 diffractometer equipped with a PHOTON100 CMOS detector. Both  $Zn_2(dobpdc)$  and  $Zn_2(dobpdc) \cdot 1.26CO_2$  were refined

in space group  $P3_121$  as inversion twins based on Flack parameter values near 0.5. Raw data were corrected for Lorenz and polarization effects using Bruker AXS SAINT software<sup>62</sup> and were corrected for absorption using SADABS.<sup>63</sup> The structures were solved using SHELXT<sup>64</sup> and refined using SHELXL<sup>65</sup> operated in the OLEX2<sup>66</sup> interface. Thermal parameters were refined anisotropically for all non-hydrogen atoms. All hydrogen atoms were placed geometrically and refined using a riding model. Disorder modeling of the  $CO_2$  molecules bound to  $Zn^{2+}$  in  $Zn_2(dobpdc) \cdot 1.26CO_2$  required the use of displacement parameter (RIGU and SIMU) and distance (DFIX) restraints.

Face-indexing was performed at the CheXray Facility at UC Berkeley with a hexanes-solvated single crystal of  $Zn_2(dobpdc)$  exposed to air. The crystal was mounted on a Bruker QUAZAR diffractometer (Mo  $K\alpha$ ,  $\lambda = 0.71073 \text{ \AA}$ ) equipped with a Bruker APEX II detector. Analysis of the crystal was performed using the Bruker APEX3 software.<sup>62</sup>

**Preparation of Samples for NMR Experiments.** Valved high-pressure 5 mm NMR tubes (Norell) were filled with activated crystals, and the tube was connected to a custom dosing apparatus (Figure 2a). Samples were first evacuated for at least 30 min before dosing with  $^{13}C$ -enriched  $CO_2$  gas (Sigma-Aldrich, 99 atom %  $^{13}C$ , <3 atom %  $^{18}O$ ) for 30 min for equilibration. For *ex situ* dosing (as performed for sample 1), the valve on the NMR tube was then closed before NMR measurements. For *in situ* dosing (sample 2), measurements were made with the sample still attached to the custom dosing manifold. Here a long piece of copper tubing was used to connect the sample inside the NMR magnet to the dosing manifold.

**NMR Experiments.** Static NMR experiments were conducted using the magnetic field strengths indicated in the figure captions. Liquid state probes and 5 mm sample tubes were used for all static measurements. MAS experiments (spectra are shown in the Supporting Information) were conducted using a DOTY 4 mm double resonance probe. For PFG NMR experiments, a Diff-30 probe and a 13-interval pulse sequence with bipolar magnetic field gradient pulses was employed (Figure S8).<sup>67</sup> Gradients were calibrated using the known self-diffusion coefficient of water at 25 °C ( $2.3 \times 10^{-9} \text{ m}^2 \text{ s}^{-1}$ ).<sup>68</sup> To test the system performance, diffusion coefficients were measured and verified against literature values for acetone, cyclohexane, toluene, and glycerol at 24 °C,<sup>68–70</sup> covering a range of self-diffusion coefficients from  $5 \times 10^{-9} \text{ m}^2 \text{ s}^{-1}$  (acetone) to  $2 \times 10^{-12} \text{ m}^2 \text{ s}^{-1}$  (glycerol). For experiments on MOF samples, the effective duration of the individual magnetic field gradient pulses ( $\delta'$ ) was 1 ms, and the maximum magnetic field gradient strength applied was 9 T  $\text{m}^{-1}$ , with sine-shaped gradient pulses used. Observation times ( $\Delta$ ) are stated in the text and were set to integer multiples of the period (20 ms) of the 50 Hz mains alternating current to mitigate potential issues from residual mains hum.<sup>31</sup> The parameter  $\tau$  was 3 ms (Figure S8). The PFG NMR decays were analyzed using eqs 3 and 4 and a fitting program written in Matlab software.  $^{13}C$  NMR chemical shifts are referenced to the ethylene carbon of neat ethanol at 57.4 ppm as a secondary reference relative to tetramethylsilane (1 vol % in deuterated chloroform) at 0.0 ppm, except for MAS experiments that are referenced to the tertiary carbon atom in adamantane at 38.5 ppm.

**Molecular Dynamics Simulations.** Molecular dynamics (MD) simulations were performed in the NVT ensemble with LAMMPS<sup>71</sup> using a time step of 1.0 fs and the Nosé–Hoover chain thermostat.<sup>72,73</sup> The dynamics of  $CO_2$  were treated using a rigid-body time integrator.<sup>74</sup> The  $CO_2$  molecules were modeled using the TraPPE force field,<sup>75</sup> and  $CO_2$ –framework interactions were modeled using a previously published force field.<sup>58</sup> The flexible lattice simulations required a molecular model for the framework atoms. Bond, angle, dihedral, and torsion parameters for linker molecules were taken from the consistent valence force field,<sup>76</sup> while  $Zn^{2+}$  ions were modeled using a cationic dummy model.<sup>77</sup> Lorenz–Berthelot mixing rules were used to calculate cross-interactions between  $Zn^{2+}$  and linker atoms. For simulations at different pressures, the framework was loaded with a number of  $CO_2$  molecules corresponding to previously published isotherms.<sup>58</sup> All MD simulations were equilibrated for 1 ns, and

production runs lasted at least 10 ns to ensure that the mean-squared displacement (MSD) became linear as a function of time. The order- $n$  algorithm<sup>78,79</sup> was used to calculate the MSD as a function of time, and the 1D self-diffusion coefficients were obtained by fitting the slope of the linear regime:  $D = \frac{1}{2} \lim_{t \rightarrow \infty} \frac{d}{dt} \langle [r(t) - r(0)]^2 \rangle$

## ■ ASSOCIATED CONTENT

### ■ Supporting Information

The Supporting Information is available free of charge on the ACS Publications website at DOI: 10.1021/jacs.7b09453.

Gas sorption, microscopy, elemental analysis, ICP, additional NMR spectra, characterization of Zn<sub>2</sub>(dobpdc) powder, and additional experimental details (PDF)

Crystallographic data for Zn<sub>2</sub>(dobpdc) (CIF)

Crystallographic data for Zn<sub>2</sub>(dobpdc)·1.26CO<sub>2</sub> (CIF)

## ■ AUTHOR INFORMATION

### Corresponding Authors

\*reimer@berkeley.edu

\*jrlong@berkeley.edu

### ORCID

Alexander C. Forse: 0000-0001-9592-9821

Velencia J. Witherspoon: 0000-0002-2718-6605

Sudi Jawahery: 0000-0001-9950-6199

Berend Smit: 0000-0003-4653-8562

Jeffrey R. Long: 0000-0002-5324-1321

### Notes

The authors declare no competing financial interest.

## ■ ACKNOWLEDGMENTS

This research was supported through the Center for Gas Separations Relevant to Clean Energy Technologies, an Energy Frontier Research Center funded by the U.S. Department of Energy (DOE), Office of Science, Office of Basic Energy Sciences, under Award DE-SC0001015. We thank the Philomathia Foundation and Berkeley Energy and Climate Institute for support of A.C.F. through a postdoctoral fellowship, the National Institutes of Health for support of P.J.M. through a postdoctoral fellowship (GM120799), and the Miller Institute for Basic Research in Science for support of J.D.M. through a postdoctoral fellowship. This work employed resources at the Advanced Light Source at Lawrence Berkeley National Lab, a user facility supported by the Director, Office of Science, Office of Basic Energy Sciences, of the DOE under Contract No. DE-AC02-05CH11231. Single-crystal X-ray diffraction equipment within the UC Berkeley CheXray Facility was supported by NIH shared Instrumentation Grant S10-RR027172. We thank ACalNet, the Aachen-California Network of Academic Exchange (DAAD Germany) for supporting a research visit of A.C.F. to RWTH Aachen University. We further thank Stefan Benders and Patrick Offer for useful discussions and assistance with PFG NMR experiments, Kristen Colwell for obtaining SEM images, Julia Oktawiec for assistance with gas adsorption measurements, Richard Bounds for assistance with the development of gas dosing equipment for *in situ* NMR experiments, and Katie R. Meihaus for providing editorial assistance.

## ■ REFERENCES

- (1) Rosi, N. L.; Kim, J.; Eddaoudi, M.; Chen, B.; O'Keeffe, M.; Yaghi, O. M. *J. Am. Chem. Soc.* **2005**, *127*, 1504.
- (2) Dietzel, P. D. C.; Morita, Y.; Blom, R.; Fjellvag, H. *Angew. Chem., Int. Ed.* **2005**, *44*, 6354.
- (3) Dietzel, P. D. C.; Panella, B.; Hirscher, M.; Blom, R.; Fjellvag, H. *Chem. Commun.* **2006**, 959.
- (4) Dietzel, P. D. C.; Blom, R.; Fjellvag, H. *Eur. J. Inorg. Chem.* **2008**, *2008*, 3624.
- (5) Zhou, W.; Wu, H.; Yildirim, T. *J. Am. Chem. Soc.* **2008**, *130*, 15268.
- (6) Bloch, E. D.; Murray, L. J.; Queen, W. L.; Chavan, S.; Maximoff, S. N.; Bigi, J. P.; Krishna, R.; Peterson, V. K.; Grandjean, F.; Long, G. J.; Smit, B.; Bordiga, S.; Brown, C. M.; Long, J. R. *J. Am. Chem. Soc.* **2011**, *133*, 14814.
- (7) Sanz, R.; Martinez, F.; Orcajo, G.; Wojtas, L.; Briones, D. *Dalt. Trans.* **2013**, *42*, 2392.
- (8) Díaz-García, M.; Sánchez-Sánchez, M. *Microporous Mesoporous Mater.* **2014**, *190*, 248.
- (9) McDonald, T. M.; Lee, W. R.; Mason, J. A.; Wiers, B. M.; Hong, C. S.; Long, J. R. *J. Am. Chem. Soc.* **2012**, *134*, 7056.
- (10) McDonald, T. M.; Mason, J. A.; Kong, X.; Bloch, E. D.; Gygi, D.; Dani, A.; Crocellà, V.; Giordanino, F.; Odoh, S. O.; Drisdell, W. S.; Vlasisavljević, B.; Dzubak, A. L.; Poloni, R.; Schnell, S. K.; Planas, N.; Lee, K.; Pascal, T.; Wan, L. F.; Prendergast, D.; Neaton, J. B.; Smit, B.; Kortright, J. B.; Gagliardi, L.; Bordiga, S.; Reimer, J. A.; Long, J. R. *Nature* **2015**, *519*, 303.
- (11) Gygi, D.; Bloch, E. D.; Mason, J. A.; Hudson, M. R.; Gonzalez, M. I.; Siegelman, R. L.; Darwish, T. A.; Queen, W. L.; Brown, C. M.; Long, J. R. *Chem. Mater.* **2016**, *28*, 1128.
- (12) Caskey, S. R.; Wong-Foy, A. G.; Matzger, A. J. *J. Am. Chem. Soc.* **2008**, *130*, 10870.
- (13) Mason, J. A.; Sumida, K.; Herm, Z. R.; Krishna, R.; Long, J. R. *Energy Environ. Sci.* **2011**, *4*, 3030.
- (14) Queen, W. L.; Hudson, M. R.; Bloch, E. D.; Mason, J. A.; Gonzalez, M. I.; Lee, J. S.; Gygi, D.; Howe, J. D.; Lee, K.; Darwish, T. A.; James, M.; Peterson, V. K.; Teat, S. J.; Smit, B.; Neaton, J. B.; Long, J. R.; Brown, C. M. *Chem. Sci.* **2014**, *5*, 4569.
- (15) Britt, D.; Furukawa, H.; Wang, B.; Glover, T. G.; Yaghi, O. M. *Proc. Natl. Acad. Sci. U. S. A.* **2009**, *106*, 20637.
- (16) Mason, J. A.; McDonald, T. M.; Bae, T.; Bachman, J. E.; Sumida, K.; Dutton, J. J.; Kaye, S. S.; Long, R. *J. Am. Chem. Soc.* **2015**, *137*, 4787.
- (17) Siegelman, R. L.; McDonald, T. M.; Gonzalez, M. I.; Martell, J. D.; Milner, P. J.; Mason, J. A.; Berger, A. H.; Bhowan, A. S.; Long, J. R. *J. Am. Chem. Soc.* **2017**, *139*, 10526.
- (18) Milner, P. J.; Siegelman, R. L.; Forse, A. C.; Gonzalez, M. I.; Runčevski, T.; Martell, J. D.; Reimer, J. A.; Long, J. R. *J. Am. Chem. Soc.* **2017**, *139*, 13541.
- (19) Lee, W. R.; Jo, H.; Yang, L.-M.; Lee, H.; Ryu, D. W.; Lim, K. S.; Song, J. H.; Min, D. Y.; Han, S. S.; Seo, J. G.; Park, Y. K.; Moon, D.; Hong, C. S. *Chem. Sci.* **2015**, *6*, 3697.
- (20) Jo, H.; Lee, W. R.; Kim, N. W.; Jung, H.; Lim, K. S.; Kim, J. E.; Kang, D. W.; Lee, H.; Hiremath, V.; Seo, J. G.; Jin, H.; Moon, D.; Han, S. S.; Hong, C. S. *ChemSusChem* **2017**, *10*, 541.
- (21) Canepa, P.; Nijem, N.; Chabal, Y. J.; Thonhauser, T. *Phys. Rev. Lett.* **2013**, *110*, 026102.
- (22) Lin, L.-C.; Kim, J.; Kong, X.; Scott, E.; McDonald, T. M.; Long, J. R.; Reimer, J. A.; Smit, B. *Angew. Chem., Int. Ed.* **2013**, *52*, 4410.
- (23) Marti, R. M.; Howe, J. D.; Morelock, C. R.; Conradi, M. S.; Walton, K. S.; Sholl, D. S.; Hayes, S. E. *J. Phys. Chem. C* **2017**, *121*, 25778.
- (24) Karger, J.; Ruthven, D. M.; Theodorou, D. N. *Diffusion in Nanoporous Materials*; Wiley-VCH, 2012.
- (25) Karger, J.; Spindler, H. *J. Am. Chem. Soc.* **1991**, *113*, 7571.
- (26) Stallmach, F.; Gröger, S.; Künzel, V.; Kärger, J.; Yaghi, O. M.; Hesse, M.; Müller, U. *Angew. Chem., Int. Ed.* **2006**, *45*, 2123.
- (27) Valiullin, R.; Porcheron, F.; Woo, H.-J.; Naumov, S.; Galvosas, P.; Monson, P. A.; Kärger, J. *Nature* **2006**, *443*, 965.

- (28) Li, J.; Park, J. K.; Moore, R. B.; Madsen, L. A. *Nat. Mater.* **2011**, *10*, 507.
- (29) Forse, A. C.; Griffin, J. M.; Merlet, C.; Carretero-Gonzalez, J.; Raji, A.-R. O.; Trease, N. M.; Grey, C. P. *Nat. Energy* **2017**, *2*, 16216.
- (30) Forman, E. M.; Pimentel, B. R.; Ziegler, K. J.; Lively, R. P.; Vasenkov, S. *Microporous Mesoporous Mater.* **2017**, *248*, 158.
- (31) Callaghan, P. T. *Translational Dynamics & Magnetic Resonance*; Oxford University Press, 2011.
- (32) Callaghan, P. T. *Principles of Nuclear Magnetic Resonance Microscopy*; Oxford University Press, 1991.
- (33) Furó, I.; Dvinskikh, S. V. *Magn. Reson. Chem.* **2002**, *40*, S3.
- (34) Topgaard, D. *J. Magn. Reson.* **2017**, *275*, 98.
- (35) Blinc, R.; Burgar, M.; Luzar, M.; Pirs, J.; Zupancic, I.; Zumer, S. *Phys. Rev. Lett.* **1974**, *33*, 1192.
- (36) Callaghan, P. T.; Le Gros, M. A.; Pinder, D. N. *J. Chem. Phys.* **1983**, *79*, 6372.
- (37) Dvinskikh, S. V.; Furo, I. *J. Magn. Reson.* **2001**, *148*, 73.
- (38) Kadi, M.; Dvinskikh, S. V.; Furo, I.; Almgren, M. *Langmuir* **2002**, *18*, 5015.
- (39) Peksa, M.; Lang, J.; Stallmach, F. *Microporous Mesoporous Mater.* **2015**, *205*, 11.
- (40) Peksa, M.; Burrekaew, S.; Schmid, R.; Lang, J.; Stallmach, F. *Microporous Mesoporous Mater.* **2015**, *216*, 75.
- (41) Bowers, C. R.; Long, H. W.; Pietrass, T.; Pines, A.; Gaede, H. C. *Chem. Phys. Lett.* **1993**, *205*, 168.
- (42) Kong, X.; Scott, E.; Ding, W.; Mason, J. A.; Long, J. R.; Reimer, J. A. *J. Am. Chem. Soc.* **2012**, *134*, 14341.
- (43) Hoffmann, H.; Debowski, M.; Müller, P.; Paasch, S.; Senkovska, I.; Kaskel, S.; Brunner, E. *Materials* **2012**, *5*, 2537.
- (44) Bon, V.; Pallmann, J.; Eisbein, E.; Hoffmann, H. C.; Senkovska, I.; Schwedler, I.; Schneemann, A.; Henke, S.; Wallacher, D.; Fischer, R. A.; Seifert, G.; Brunner, E.; Kaskel, S. *Microporous Mesoporous Mater.* **2015**, *216*, 64.
- (45) Chen, S.; Lucier, B. E. G.; Boyle, P. D.; Huang, Y. *Chem. Mater.* **2016**, *28*, 5829.
- (46) Zhang, Y.; Lucier, B. E. G.; Huang, Y. *Phys. Chem. Chem. Phys.* **2016**, *18*, 8327.
- (47) Lu, Y.; Lucier, B. E. G.; Zhang, Y.; Ren, P.; Zheng, A.; Huang, Y. *Phys. Chem. Chem. Phys.* **2017**, *19*, 6130.
- (48) Winn, E. B. *Phys. Rev.* **1950**, *80*, 1024.
- (49) Tovar, T. M.; Zhao, J.; Nunn, W. T.; Barton, H. F.; Peterson, G. W.; Parsons, G. N.; Levan, M. D. *J. Am. Chem. Soc.* **2016**, *138*, 11449.
- (50) Salles, F.; Jobic, H.; Devic, T.; Llewellyn, P. L.; Serre, C.; Ferey, G.; Maurin, G. *ACS Nano* **2010**, *4*, 143.
- (51) Jobic, H.; Laloue, N.; Laroche, C.; van Baten, J. M.; Krishna, R. *J. Phys. Chem. B* **2006**, *110*, 2195.
- (52) Fernandez, M.; Karger, J.; Freude, D.; Pampel, A.; van Baten, J. M.; Krishna, R. *Microporous Mesoporous Mater.* **2007**, *105*, 124.
- (53) Alavi, S.; Dornan, P.; Woo, T. K. *ChemPhysChem* **2008**, *9*, 911.
- (54) Rowland, R. S.; Taylor, R. J. *Phys. Chem.* **1996**, *100*, 7384.
- (55) Bondi, A. J. *Phys. Chem.* **1964**, *68*, 441.
- (56) Øien, S.; Wragg, D.; Reinsch, H.; Svelle, S.; Bordiga, S.; Lamberti, C.; Lillerud, K. P. *Cryst. Growth Des.* **2014**, *14*, 5370.
- (57) Lin, L.-C.; Lee, K.; Gagliardi, L.; Neaton, J. B.; Smit, B. *J. Chem. Theory Comput.* **2014**, *10*, 1477.
- (58) Mercado, R.; Vlasisavljevich, B.; Lin, L.-C.; Lee, K.; Lee, Y.; Mason, J. A.; Xiao, D. J.; Gonzalez, M. I.; Kapelewski, M. T.; Neaton, J. B.; Smit, B. *J. Phys. Chem. C* **2016**, *120*, 12590.
- (59) Dietzel, P. D. C.; Johnsen, R. E.; Fjellvag, H.; Bordiga, S.; Groppo, E.; Chavan, S.; Blom, R. *Chem. Commun.* **2008**, *2*, 5125.
- (60) Pato-Doldán, B.; Rosnes, M. H.; Dietzel, P. D. C. *ChemSusChem* **2017**, *10*, 1710.
- (61) Gonzalez, M. I.; Mason, J. A.; Bloch, E. D.; Teat, S. J.; Gagnon, K. J.; Morrison, G. Y.; Queen, W. L.; Long, J. R. *Chem. Sci.* **2017**, *8*, 4387.
- (62) SAINT, APEX<sub>2</sub>, and APEX<sub>3</sub> Software for CCD Diffractometers, Bruker Analytical X-ray Systems Inc., Madison, WI, 2014.
- (63) Sheldrick, G. M. SADABS, program for empirical absorption correction of area detector data; University of Göttingen, Germany.
- (64) Sheldrick, G. M. *Acta Crystallogr., Sect. A: Found. Adv.* **2015**, *71*, 3.
- (65) Sheldrick, G. M. *Acta Crystallogr., Sect. C: Struct. Chem.* **2015**, *71*, 3.
- (66) Dolomanov, O. V.; Bourhis, L. J.; Gildea, R. J.; Howard, J. A. K.; Puschmann, H. *J. Appl. Crystallogr.* **2009**, *42*, 339.
- (67) Cotts, R. M.; Hoch, M. J. R.; Sun, T.; Markert, J. T. *J. Magn. Reson.* **1989**, *83*, 252.
- (68) Holz, M.; Heil, S. R.; Sacco, A. *Phys. Chem. Chem. Phys.* **2000**, *2*, 4740.
- (69) Krüger, G. J.; Weiss, R. Z. *Naturforsch. Tl. A* **1970**, *25*, 777.
- (70) Burnett, L. J.; Harmon, J. F. *J. Chem. Phys.* **1972**, *57*, 1293.
- (71) Plimpton, S. J. *Comput. Phys.* **1995**, *117*, 1.
- (72) Nosé, S. A. *Mol. Phys.* **1984**, *52*, 255.
- (73) Hoover, W. G. *Phys. Rev. A: At., Mol., Opt. Phys.* **1985**, *31*, 1695.
- (74) Kamberaj, H.; Low, R. J.; Neal, M. P. *J. Chem. Phys.* **2005**, *122*, 224114.
- (75) Wick, C. D.; Martin, M. G.; Siepmann, J. I. *J. Phys. Chem. B* **2000**, *104*, 8008.
- (76) Dauber-Osguthorpe, P.; Roberts, V. A.; Osguthorpe, D. J.; Wolff, J.; Genest, M.; Hagler, A. T. *Proteins: Struct., Funct., Genet.* **1988**, *4*, 31.
- (77) Duarte, F.; Bauer, P.; Barrozo, A.; Amrein, B. A.; Purg, M.; Åqvist, J.; Kamerlin, S. C. L. *J. Phys. Chem. B* **2014**, *118*, 4351.
- (78) Frenkel, D.; Smit, B. *Understanding Molecular Simulation: From Algorithms to Applications*; Elsevier Science, 2002.
- (79) Dubbeldam, D.; Ford, D.; Ellis, D.; Snurr, R. *Mol. Simul.* **2009**, *35*, 1084.